Simulation of light delivery for photoacoustic breast imaging using the handheld probe

Guohe Wang (王国鹤), Honghong Zhao (赵宏宏), Qiushi Ren (任秋实), and Changhui Li (李长辉)***

Department of Biomedical Engineering, College of Engineering, Peking University, Beijing 100871, China

**Corresponding author: chli@pku.edu.cn; **corresponding author: renqsh@coe.pku.edu.cn*

Received January 12, 2014; accepted March 27, 2014; posted online April 30, 2014

The photoacoustic tomography by using the handheld probe has a great potential in clinical breast imaging. However, the shape of the probe limits the choice of light delivery in this setup. In this letter, we study two commonly used illumination types for handheld probe: bright-field illumination and dark-field illumination. Our results demonstrate several parameters have important impact on the photon fluence in deep breast tissue. The results will help to optimize the design of the photoacoustic breast imaging system with a handheld probe.

OCIS codes: 170.0170, 110.0110, 290.0290.
doi: 10.3788/COL201412.051703.

The breast cancer is a primary health threat to women globally. Nowadays X-ray mammography and ultrasound are widely used in the breast cancer diagnosis. However, the ionizing radiation of X-ray mammography has the potential hazard causing carcinogenic risk, and ultrasound has not enough contrast and specificity for early cancer detection[1]. Photoacoustic tomography (PAT) is an emerging nonradioactive imaging technique with high optical contrast and fine spatial resolution in deep tissue by combining diffusive photons absorption with ultrasound detection[2−5]. Due to the unique structure and relative simple tissue composition, breast imaging is always an important research field of PAT[6−8]. Preclinical study demonstrated PAT has a great potential to be a clinical non-invasive imaging method for diagnosis or monitoring of breast cancer[9,10].

Since the handheld ultrasound probe has been clinically widely used with great convenience, combining optical illumination with ultrasound probe becomes an important design for PAT[11−14]. To achieve a higher signal-to-noise ratio (SNR) at the depth of interest, it is very important to have enough photons to reach the location while keeping the laser power under safety standard. Unlike many other PAT systems, the unique shape of the probe and its clinical requirement demand an especially compact illumination design within a very limited space. Several researches have demonstrated that illumination parameters can have important affection on photon transportation in PAT[15,16]. In this letter, we focused on two illumination types that are generally used in handheld based PAT systems: bright-field and dark-field illuminations[17,18]. The Monte Carlo (MC) simulations were used to study the influence of the illumination parameters in both types on the light distribution in deep breast tissue (0.5−3 cm under skin). The results will help to optimize the design of the handheld-based PA imaging system for breast imaging.

The schematic diagrams of the breast tissue model and PAT probe are shown in Fig. 1. The breast tissue was considered to be a two layer system: skin layer and subcutaneous fat layer. The subcutaneous fat layer was considered as semi-infinitely deep. The rectangular shaped handheld probe was immersed in water that served as the coupling medium. In this letter, we chose the illumination laser as a near infrared (NIR) light source at 757 nm. The optical properties of the breast tissue and coupling medium at this wavelength were given in Table 1.

Two illumination types were studied: bright-field and dark-field illumination, as described in Fig. 1. In the bright-field case, the rectangular beam normally shined on the tissue surface right below the probe head. This illumination can be achieved by several methods, such as customized probes with optical fibers inside or using a reflector[15,17]. The primary parameters in this simulation are the width (w) and the length (l) of the illumination beam. In the dark-field case, two rectangular beams obliquely launched from both long sides of the probe. The illumination parameters include the

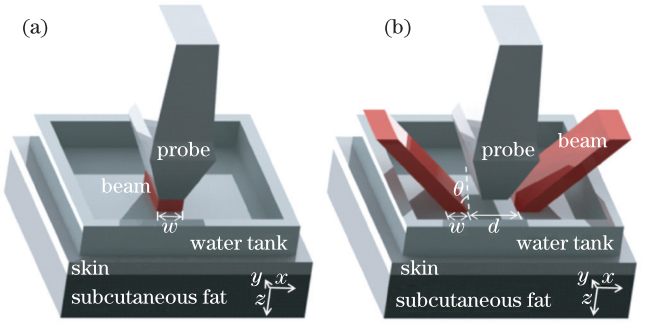

Fig. 1. (Color online) Configurations of the two illumination types and the biological tissue. (a) The bright-field design; (b) the dark-field design. The y-axis points outward.

Table 1. Optical Properties of the Breast Model at 757-nm Wavelength[9,10]

Layer	Refractive Index	μ_a(cm^{-1})	μ_s(cm^{-1})	g	Thickness (cm)
Water	1.33	—	—	—	—
Skin	1.4	0.2	75	0.8	0.2
Subcutaneous Fat	1.4	0.04	100	0.9	—

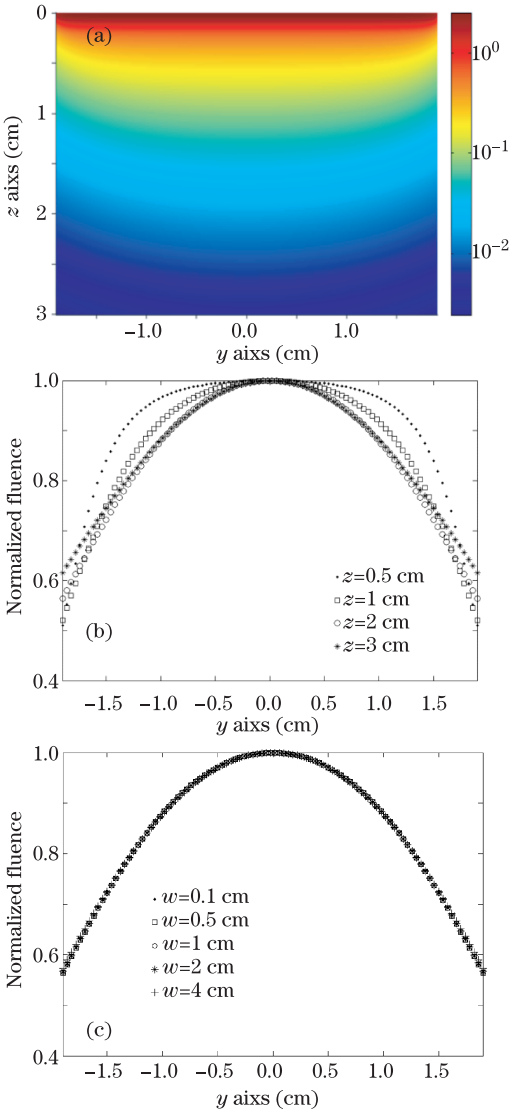

Fig. 2. (Color online) The uniformity of the light distribution along y-axis (a) the light distribution in the whole image plane (the 3D distribution of the photon density is available online created by ImageJ (National Institutes of Health)), (b) the normalized light distributions along y-axis at z = 0.5–3 cm. (c) The normalized light distributions along y-axis with different beam widths.

incident angle (θ), the widths (w'), the length (l') of the two beams, and the interval (d) between them on skin. In this letter, we employed the MC simulation method to study how these parameters of illumination configurations affect the photon distribution under the probe. In the simulation, the tissue surface is set as $x-y$ plane, and z-axis is the normal of the surface pointing to the tissue. The size of the probe is based on a 5−14 MHz ultrasound probe (L14-5/38, Ultrasonix, Canada) with a length of 3.8 cm. The ultrasound array aligned parallel to y-axis, that is, the B-scan imaging plane is in the y-z plane. The point on the skin surface right below the center of the ultrasound probe was set as the origin of the coordinate system. The number of photon packets in each MC simulation was 100 million. The incident pulse power density on the surface in all simulations is 1.0 mJ/cm^2.

Given the illumination parameters, we firstly used MC to get the photon distribution for a single beam light, which serves the Green's function ($G(x, y, z)$). Since the optical property in this model is invariant in x and y directions, and the illuminating beams are all collimated, then the photon distribution ($C(x, y, z)$) of the finite-size illumination beams in both types can be computed by the convolution of their Green's functions and illumination patterns:

$$C(x,y,z) = \iint\limits_{x',y' \in S} G(x-x', y-y', z) * S(x', y') \mathrm{d}x' \mathrm{d}y', \tag{1}$$

where $S(x, y)$ represents the rectangular intensity profile illuminated on the tissue surface. This equation is solved by numerical integration. For different illumination parameters, we solve Eq. (1) by choosing corresponding $G(x, y, z)$ and $S(x, y)$.

Since the field of view for a typical handheld probe is a narrow plane just under the probe head, we therefore only studied the photon distribution along y-axis and z-axis in the imaging plane of the probe. In the letter, we assumed the length of the laser beams was the same as the length of the probe.

Due to the finite size of the illumination area, photon fluence in tissue varies along the y-axis. Since the PA signal is proportional to the production of the absorption coefficient and light fluence, quantitative PAT desired a uniform or known distribution of light in tissue. Here, various beam sizes and illumination angles were used in simulation to study how these parameters affect the radiation field along y axis.

For type 1 a rectangular laser beam normally illuminated on the skin. We simulated different widths of the beam. The first case used the width of w=0.1 cm. The photon fluence distribution in the imaging plane was shown in Fig. 2(a), which was plotted in log scale. The result indicates that there is a slight decline from the center to edge along the y axis at a given depth. To evaluate the uniformity at different depths, the light fluence along y-axis at four depths (z=0.5, 1, 2, 3 cm) were normalized to their maximum values at each depth respectively, as shown in Fig. 2(b). For instance, at z= 0.5 cm, the maximum decrease of the fluence from the center to the edges was about 49%. From z=0.5 to 3 cm, the fluence declined more and more quickly away from the center but more and more slowly approaching to the edges. Then,

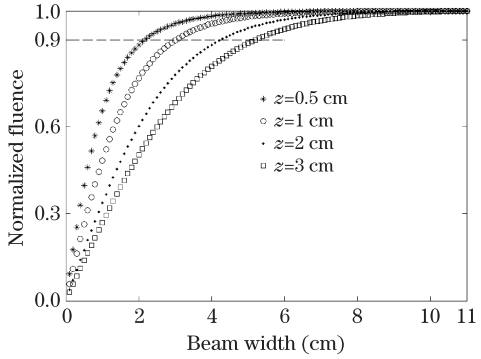

Fig. 3. Fluence versus depth with different widths of the laser beam in type 1.

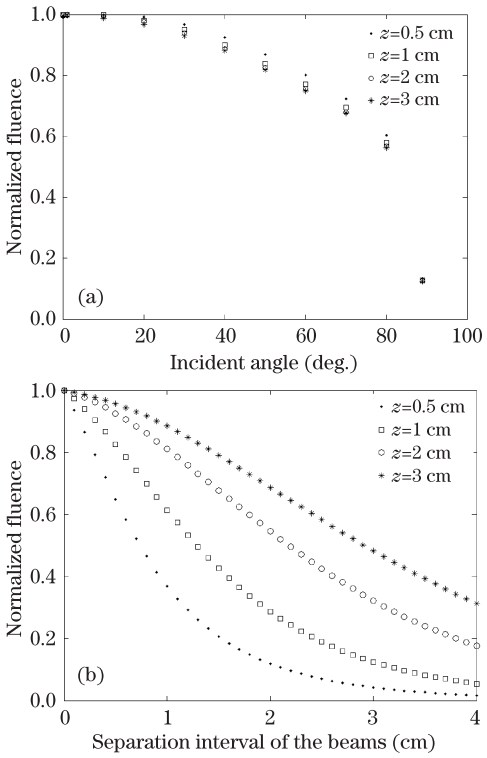

Fig. 4. Normalized fluence variation at different depths with (a) the incident angle and (b) the separation interval of the beams in type 2.

different beam widths from 0.1 to 4 cm were simulated. The fluence distributions at $z = 2$ cm were chosen as the representative of the uniformity studies. As shown in Fig. 2(c), the fluence distributions with different beam widths which were normalized to their maximum fluence values at each width respectively nearly coincided, indicating that the width of the illumination light had little influence on the fluence uniformity at this depth. Similar results were also obtained at other depths. For type 2 the influences of the incident angle (θ), beam width (w'), and the dark-field separation interval (d) were all studied. The normalized fluence distributions at $z = 2$ cm under these different parameters also present a similar behavior with type 1, i.e., the fluence variation along y-axis is insensitive to the illumination parameters. Therefore, the two illumination types and those parameters of beam width, illumination angle, and dark-field interval have little influence on the uniformity patterns along y direction in the imaging plane.

We went on studying how the illumination parameters affect the fluence distribution at different depths. Parameters including beam width, incident angle, and dark-field separation interval were simulated. Here, we only present the results at the center z-axis, while similar results were obtained at other positions.

In type 1 case, we simulated fluence with different widths of the laser beam from 0.1 to 11 cm. In Fig. 3, we plotted the fluence vs. beam width at different depths, and at each depth, we normalized the fluence to its maximum value. With no surprise, the result shows that the fluence increases as the width of the beam increases. However, the increase of the fluence will slow down significantly after the width reaches certain scale. For instance, at z=3 cm, there will be no big difference in fluence once the beam width becomes wider than 5 cm.Here, we choose 90 % of the maximum in fluence as the reference level. Based on simulation results, we obtained an empirical relationship between the required beam width w (cm) and the imaging depth (z=0.5 to 3 cm) to reach the reference level, which is fitted by using the least-squares method:

$$w \approx 2.82 * z^{0.52}. \quad (2)$$

In type 2 case, the influence of the incident angle, the interval of the two beams and the widths of them were studied. Firstly, the incident angle varied from 0° to 89°. The separation interval of the beams was set as d=0.1 cm, and the illumination width of each side was set as $w' = 0.5$ cm. The simulation results were normalized to the maximum fluence value at each depth respectively. Figure 4(a) presents the fluence variation with different incident angles at z= 0.5, 1, 2, 3 cm. The fluence has the maximum at around 0°−20° and then declines monotonously as the incident angles increases. Secondly, different separation intervals of the beams from 0 to 4 cm were simulated with $w' = 0.5$ cm and θ=30°. The result was shown in Fig. 4(b). The fluence drops very quickly as the dark-field interval becomes broader. Finally, the simulation with the width of the two side beams from 0.1 to 5.5 cm were studied, where fixing θ= 30° and d =0.1 cm. Similar to the analysis in type 1, here we also use 90% of the maximum fluence as the reference level, and a similar empirical relationship between the beam width and the imaging depth is obtained. In order to be consistent with Eq. (2), we choose W=2w' (cm) instead of w'. The fitted formula is

$$W \approx 2.81 * z^{0.52}. \quad (3)$$

From the results, it is obviously that small incident angle, narrow separation interval and wide beams lead to more photons to be deposited under the probe. However, the conditions of small incident angle and narrow dark-field usually cannot be satisfied simultaneously due to the probe shape. A balance between the incident angle and the dark-filed interval should be made. The light distribution in the breast tissue under the combination of varied incident angles (from 0° to 89°) and intervals of the dark filed (from 0 to 4 cm) were simulated.

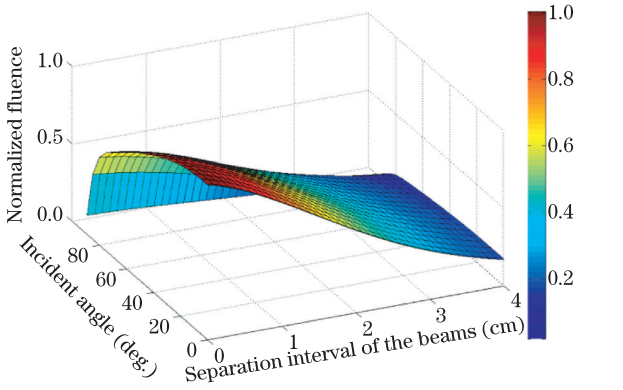

Fig. 5. (Color online) Normalized fluence distributions with the combination of varied incident angles and dark-filed intervals.

Figure 5 shows the variation of the fluence distributions normalized to the maximum value with different parameter combinations, where the illumination pattern was set 3.8×0.5 (cm) and the imaging depth was set at 2 cm. Designers could find out the optimized combination of incident angle and the dark-field interval according to the result.

In conclusion, in order to develop PAT with handheld probe for breast imaging, we employ MC simulations to study light distributions with two different illumination types. In our study, the light beam size, illumination angle, and the separation interval of the beams are all simulated. As long as the length of the laser beams is designed identical as that of the ultrasound array, the uniform of the fluence distribution along the y-axis is acceptable and is insensitive to other illumination parameters. Besides, our study provides the optimal illumination strategy in each type. In type 1 the photon deposition increases as the width of the beam becomes broader. However, the fluence approaches saturation when the width becomes enough wide. An optimal laser beam width given by Eq. (2) can not only generate a high PA signal but also avoid unnecessary light exposure and heating of the tissue. In type 2 the wider beam will help the fluence increase and an empirical formula Eq. (3) is provided too. Moreover, the fluence increases when the incident angle decreases and the width of the dark-filed interval become narrower, but a balance between them needs to make in practical application. According to Fig. 5, designers can seek an optimal combination of the incident angle and the separation interval. Besides, the type 1 can be regarded as the extreme form of type 2, and has the maximum light fluence. Therefore, although type 2 design is more practically convenient, type 1 has better imaging performance for breast imaging. This letter will help researchers and manufactures to design and optimize the PAT probe in their applications.

This work was sponsored by the National Key Instrumentation Development Project (No. 2011YQ030114), the National Basic Research Program of China (973 Program) (No. 2011CB707502), and the National Natural Science Foundation of China (No. 61078073).

References

1. W. Teh, A. Wilson, A. Evans, H. Burrell, S. Pinder, and I. Ellis, Clinical Radiology **55,** 390 (2000).
2. L. Wang and S. Hu, Science **335,** 1458 (2012).
3. C. Li and L. Wang, Phys. Med. Biol. **54,** R59 (2009).
4. S. Ye, J. Yang, J. Xi, Q. Ren, and C. Li, Chin. Opt. Lett. **10,** 121701 (2012).
5. Z. Ren, G. Liu, and Z. Huang, Chin. Opt. Lett. **11,** 21701 (2013).
6. M. Pramanik, G. Ku, C. Li, and L. Wang, Med. Phys. **35,** 2218 (2008).
7. S. Manohar, S. E. Vaartjes, J. C. Hespen, J. M. Klaase, F. M. Engh, W. Steenbergen, and T. G. Leeuwen, Opt. Express **15,** 12277 (2007).
8. L. Wang, Med. Phys. **35,** 5758 (2008).
9. S. A. Ermilov, T. Khamapirad, A. Conjusteau, M. H. Leonard, R. Lacewell, K. Mehta, T. Miller, and A. A. Oraevsky, J. Biomed. Opt. **14,** 024007 (2009).
10. R. A. Kruger, C. M. Kuzmiak, R. B. Lam, D. R. Reinecke, S. P. Del Rio, and D. Steed, Med. Phys. **40,** 113301 (2013).
11. J. J. Niederhauser, M. Jaeger, R. Lemor, P. Weber, and M. Frenz, IEEE Trans. Med. Imag. **24,** 436 (2005).
12. C. Kim, T. N. Erpelding, L. Jankovic, M. D. Pashley, and L. Wang, Biomed. Opt. Express **1,** 278 (2010).
13. D. Yang, D. Xing, Y. Tan, H. Gu, and S. Yang, Appl. Phys. Lett. **88,** 174101 (2006).
14. L. Nie, M. Chen, X. Sun, P. Rong, N. Zheng, and X. Chen, Nanoscale **6,** 1271 (2014).
15. V. Periyasamy and M. Pramanik, J. Biomed. Opt. **18,** 106008 (2013).
16. Z. Xie, L. Wang, and H. Zhang, Appl. Opt. **48,** 3204 (2009).
17. L. G. Montilla, R. Olafsson, D. R. Bauer, and R. S. Witte, Phys. Med. Biol. **58,** N1 (2013).
18. C. Kim, T. N. Erpelding, K. Maslov, L. Jankovic, W. J. Akers, L. Song, S. Achilefu, J. A. Margenthaler, M. D. Pashley, and L. Wang, J. Biomed. Opt. **15,** 046010 (2010).